ACS APPLIED MATERIALS & INTERFACES

www.acsami.org

Research Article

Interfacial Engineering at Quantum Dot-Sensitized TiO_2 Photoelectrodes for Ultrahigh Photocurrent Generation

Tea-Yon Kim,[▽] Byung Su Kim,[▽] Jong Gyu Oh, Seul Chan Park, Jaeyoung Jang, Thomas W. Hamann, Young Soo Kang, Jin Ho Bang,* Sixto Giménez,* and Yong Soo Kang*

Cite This: *ACS Appl. Mater. Interfaces* 2021, 13, 6208–6218

Read Online

ACCESS | Metrics & More | Article Recommendations | Supporting Information

ABSTRACT: Metal oxide semiconductor/chalcogenide quantum dot (QD) heterostructured photoanodes show photocurrent densities >30 mA/cm^2 with ZnO, approaching the theoretical limits in photovoltaic (PV) cells. However, comparative performance has not been achieved with TiO_2. Here, we applied a TiO_2(B) surface passivation layer (SPL) on TiO_2/QD (PbS and CdS) and achieved a photocurrent density of 34.59 mA/cm^2 under AM 1.5G illumination for PV cells, the highest recorded to date. The SPL improves electron conductivity by increasing the density of surface states, facilitating multiple trapping/detrapping transport, and increasing the coordination number of TiO_2 nanoparticles. This, along with impeded electron recombination, led to enhanced collection efficiency, which is a major factor for performance. Furthermore, SPL-treated TiO_2/QD photoanodes were successfully exploited in photoelectrochemical water splitting cells, showing an excellent photocurrent density of 14.43 mA/cm^2 at 0.82 V versus the Reversible Hydrogen Electrode (RHE). These results suggest a new promising strategy for the development of high-performance photoelectrochemical devices.

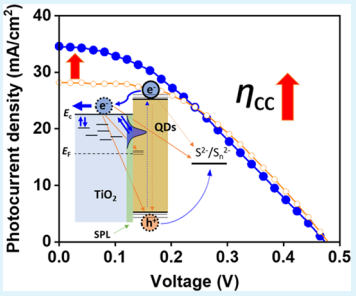

KEYWORDS: *TiO_2/QD, photoanode, photoelectrochemical cells, surface passivation layer, surface state, charge collection, photocurrent density*

1. INTRODUCTION

Chalcogenide quantum dots (QDs) have attracted much attention as building blocks for next-generation light-harvesting devices due to their outstanding optical characteristics such as a wide light absorption range over the near-IR regions and high extinction coefficient.[1−5] Typical examples of such light-harvesting devices include photovoltaic (PV) cells and photoelectrochemical (PEC) water splitting cells, consisting of light-harvesting materials deposited on a mesoporous n-type semiconductor layer of TiO_2, ZnO, or SnO_2; an electrolyte; and a counter electrode.[6−8]

Over the last 5 years, high photocurrent densities greater than 30 mA/cm^2 have been reported for PV cells using metal oxide/chalcogenide QD heterostructured photoanodes having high light-harvesting ability (Figure 1). For instance, ZnO/chalcogenide QDs have led to ultrahigh photocurrent densities in PV cells, with a record value of 39 mA/cm^2, closely approaching the theoretical photocurrent density (44 mA/cm^2) for the 1.1 eV band gap of such QDs.[9] However, TiO_2/chalcogenide QD heterostructures have been struggling to reach photocurrent densities greater than 30 mA/cm^2, mostly due to the lower electron conductivity of TiO_2 compared to ZnO.[10] In this work, we achieved a photocurrent density close to 35 mA/cm^2, the highest recorded to date (Figure 1).

Chalcogenide QDs have been actively exploited for the generation of solar hydrogen in PEC water splitting cells due to their outstanding water durability compared to other light-harvesting materials such as metalorganic dyes and halide perovskites.[18,19] In this regard, TiO_2/chalcogenide QD photoanodes are much more attractive for PEC hydrogen generation compared to ZnO/chalcogenide QDs due to the excellent stability of TiO_2 in strong-base electrolyte conditions.[20] Therefore, the development of TiO_2/chalcogenide QD photoanodes showing a high photocurrent density greater than 30 mA/cm^2 in PV cells is extremely attractive for PEC applications.

To design the optimal architecture of photoanodes with TiO_2/chalcogenide QDs for high photocurrents, enhancement of both charge transfer kinetics at the TiO_2/chalcogenide QD interface and charge transport via the TiO_2 films should be simultaneously considered.[21] As a general strategy, the introduction of a surface passivation layer (SPL) on TiO_2 film has led to significant improvements in sensitized PV cells.[22,23] Particularly, $TiCl_4$ treatment to form a TiO_2 SPL at the interface of TiO_2/light-harvesting materials has led to an about 10−30% photocurrent density increase.[24] In dye-sensitized solar cells (DSSCs) with a SPL, performance

Received: October 28, 2020
Accepted: January 20, 2021
Published: February 1, 2021

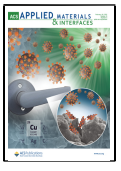

https://dx.doi.org/10.1021/acsami.0c19352
ACS Appl. Mater. Interfaces 2021, 13, 6208−6218

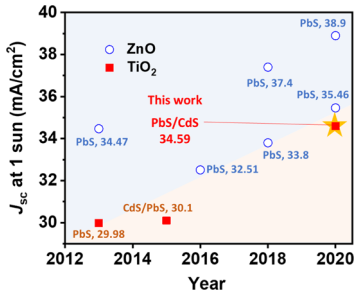

Figure 1. Short-circuit current density (J_{sc}) for PV cells since 2013 with semiconductor/chalcogenide QD photoanodes with ZnO (blue empty circles) and TiO_2 (red filled squares) at a 1 sun condition.[9,11−17] The yellow star indicates the performance of this work with TiO_2.

enhancement has been attributed to the improved electron injection, mostly because of driving force enhancement through the conduction band (CB) shift of TiO_2 and suppression of electron recombination at the TiO_2/dye interface.[24] However, changes in electron transport induced by SPLs have been reported to be minimal due to the high diffusion length of electrons through the mesoporous TiO_2 layer (20−25 μm with I_3^-/I^- redox couples and 10−12.5 μm for water oxidation[25,26]) compared to the film thickness (~13 μm).[24,27,28] Conversely, multiple electron recombination pathways have been reported for TiO_2/chalcogenide QD photoanodes due to the complex distribution of energy states as well as the ultrafast electron injection rate to TiO_2 ($<10^{-9}$ s).[3,18,29] Therefore, it is expected that the effects of the SPL on the functional performance of TiO_2/QD photoanodes will be significantly different from those of conventional TiO_2/dye photoanodes, although explicit effects on transport properties have not been completely elucidated.

Electron transport in mesoporous TiO_2 films is commonly interpreted with the trap state-mediated transport model with multiple trapping/detrapping events.[30] In semiconductors, shallow traps in a band gap significantly affect electron transport and are typically located 0.5−1.0 eV below the CB.[31] Therefore, the deposition of the SPL impacts the population and distribution of trap states of TiO_2 with a concomitant effect on the TiO_2/chalcogenide QD interface. During SPL formation on the TiO_2 film, the surface states, which are localized and generated by chemical surface treatment, can affect electron transport.[32] The surface states of TiO_2 are formed mainly at the trap state area 0.3−0.4 eV below the CB and originate mainly from undercoordinated Ti^{4+} atoms on the anatase TiO_2 surface.[33] It is well-known that charge transfer at the interface of the mesoporous semiconductor/solution is affected by surface states.[34−36] However, even though the increase in the density of surface trap states in relation to deposition of the TiO_2 SPL has been extensively reported, its effects on electron transport through mesoporous TiO_2 films are uncertain.[24,28,37] Additionally, changes in film morphology during the formation of the SPL have a significant impact on the electron transport of TiO_2 films.[30] Therefore, the effects of the SPL on electron transport, as well as on energetics and the morphology of the photoelectrodes, should be precisely tuned to improve the photocurrent density.

Herein, we achieved a photocurrent density of 34.59 mA/cm^2 in PV cells with a 0.18 cm^2 active area and 14.43 mA/cm^2 in PEC water splitting cells with an active area of 1.33 cm^2 at 1 sun condition with about 20% enhancement (compared to the reference samples) by hydrothermal treatment of $TiCl_4$ to form an SPL on the TiO_2/PbS-CdS QD photoanodes. Based on the results of photocurrent densities on PV cells and PEC water splitting cells, the SPL facilitates electron conductivity of mesoporous TiO_2 films by increasing the density of surface states and the coordination number of TiO_2 nanoparticles (NPs). The increased electron conductivity is mostly due to an increase in surface states for multiple trapping/detrapping transport through TiO_2 films, which was quantified in terms of the chemical diffusion coefficient. The suppression of electron recombination was also observed for the SPL. Therefore, we conclude that the main effects of the SPL on the photocurrent density of TiO_2/PbS-CdS QD photoanodes are related to improved charge collection efficiency (η_{cc}), driven by enhancement of electron transport and suppression of electron recombination.

2. EXPERIMENTAL SECTION

2.1. Materials. All chemicals and materials were purchased from a commercial company and were used without further purification. Acetonitrile (ACN), acetone (ACT), deionized water (DI water), ethanol (EtOH), methanol (MeOH), cadmium acetate dihydrate ($Cd(CH_3COO)_2{\cdot}2H_2O$), copper(II) sulfate ($CuSO_4$), hydrochloride acid (HCl), lead nitrate ($Pb(NO_3)_2$), potassium chloride (KCl), sulfur (S), sodium sulfide (Na_2S), sodium sulfide nonahydrate ($Na_2S{\cdot}9H_2O$), sodium sulfite (Na_2SO_3), sodium thiosulfate ($Na_2S_2O_3$), titanium(IV) chloride ($TiCl_4$), and zinc acetate dihydrate ($Zn(CH_3COO)_2{\cdot}2H_2O$) were purchased from Sigma Aldrich. Fluorine-doped tin oxide (FTO) glass substrates (TEC-15) were purchased from Pilkington (U.K.). Titanium dioxide (TiO_2) nanoparticulate pastes were purchased from Dyesol (30NR-T, Australia) and CCIC (PST-18 NR, PST-400C, Japan).

2.2. Preparation of Mesoporous TiO_2/PbS-CdS QD Photoanodes and Counter Electrodes. An FTO glass substrate was cleaned in a two-step sonication process with an aqueous detergent solution for 1 h (2% Hellmanex III in DI water, v/v) and subsequently with an organic solvent mixture (EtOH and ACT, 1:1, v/v). The cleaned FTO substrates were used for all working- and counter electrodes. For the purification of $TiCl_4$, a 0.05 mol of $TiCl_4$ solution was slowly added dropwise to an HCl solution in a 1:5 ratio at −20 °C.[38] A TiO_2 blocking layer (~20 nm) on the FTO substrate of the working electrode was treated using the hydrothermal method with a 40 mM $TiCl_4$ aqueous solution at 70 °C for 30 min. After rinsing with DI water and EtOH, the working electrode was sintered at 450 °C for 30 min. This process was repeated to form double blocking layers. Next, two layers of TiO_2 NPs and one layer of TiO_2 light-scattering particles (~400 nm, CCIC) were doctor-bladed onto the blocking layer-coated FTO glass and sintered at 450 °C for 30 min. The thickness of the photoanode was around 12 μm. For the PT20 and PT30 samples, $TiCl_4$ treatment was conducted on neat TiO_2 films with 20 and 30 nm NPs (termed T20 and T30, hereafter) using the hydrothermal method with a 40 mM $TiCl_4$ aqueous solution at 70 °C for 18 min and then sintered at 450 °C for 30 min before rinsing with DI water and EtOH.

For the photoanode used in both PV cells and PEC water splitting cells, the co-sensitization of PbS and CdS QDs was applied in this work using the successive ionic layer adsorption and reaction (SILAR) method for the direct growth of QDs on the surface of TiO_2 films. The detailed synthetic method of QDs was followed according to our previous study with slight modifications.[39] First, the TiO_2 films were immersed in a 0.1 M $Cd(CH_3COO)_2{\cdot}2H_2O$ solution in MeOH for a few seconds for the precoating of QDs. For PbS QD deposition, the films were immersed in a Pb^{2+} (0.02 M $Pb(NO_3)_2$ in MeOH) and a S^{2-} solution (0.02 M $Na_2S{\cdot}9H_2O$ in MeOH/water (1:1, v/v)) in succession. The deposition of PbS QD was repeated three times. TiO_2/PbS films were then immersed in a Cd^{2+} (0.1 M $Cd(CH_3COO)_2{\cdot}2H_2O$ in MeOH) and a S^{2-} solution (0.1 M $Na_2S{\cdot}9H_2O$ in MeOH/water (1:1, v/v)) repeatedly for six times for CdS

https://dx.doi.org/10.1021/acsami.0c19352
ACS Appl. Mater. Interfaces 2021, 13, 6208−6218

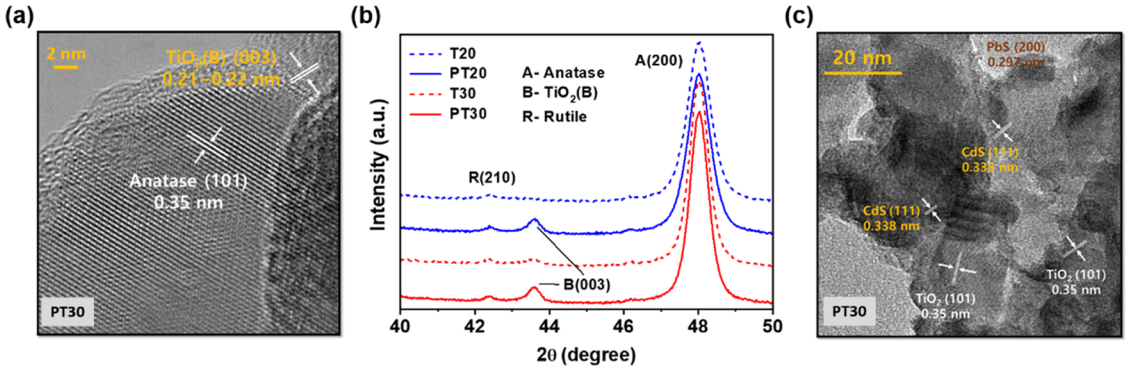

Figure 2. (a) HR-TEM image of PT30 with typical lattice distances of anatase (101), rutile (210), and TiO_2(B) (003). (b) XRD patterns of TiO_2 films indicating the peaks for anatase A (200) at 2θ = 48.0°, rutile R (210) at 2θ = 42.5°, and TiO_2(B)(003) at 2θ = 43.5°. (c) TEM images with typical lattice distances of PbS(200) and CdS(111) QDs deposited on PT30.

deposition. For the ZnS passivation layer, TiO_2/QD heterostructured electrodes were additionally immersed in a Zn^{2+} (0.1 M Zn-$(CH_3COO)_2{\cdot}2H_2O$ in MeOH) and a S^{2-} solution (0.1 M $Na_2S{\cdot}9H_2O$ in MeOH/water (1:1, v/v)) twice repeatedly. Between each step, a cleaning process should be conducted for the production of high-quality QD films by rinsing the films with MeOH and DI water to remove impurities during the successive deposition. The immersion period for each step was 1 min per solution.

The fabrication method used to create the Cu_xS counter electrode (CE) for PV cells was adopted from previous studies.[40,41] Copper sulfides were deposited on FTO glass by the chemical bath deposition (CBD) method. A mixture of 0.1 M $CuSO_4$ and $Na_2S_2O_3$ aqueous solutions was used for the deposition of Cu_xS films. Then, FTO was dipped in the solution at 70 °C for 3 h at pH 3, rinsed with DI water and EtOH, and dried using N_2 gas. The as-prepared film was annealed at 130 °C for 30 min under ambient conditions. For PEC water splitting cells, a 2.5 cm × 2.5 cm commercial Pt plate was used.

2.3. Fabrication of PV Cells and PEC Water Splitting Cells. For PV cells, we employed the sandwich fabrication method using the Cu_xS CE with two holes predrilled for electrolyte injection and the QD-photoanode. A 25 μm thick Surlyn film was placed between the two electrodes as a spacer, and the electrolyte composed of 2.0 M S, Na_2S, and KCl in aqueous solution was injected into this space. The holes were then covered up using a Surlyn film and cover glass for finishing.

In PEC water splitting cells, a Pt plate (2.5 cm × 2.5 cm) and a Ag/AgCl (3 M KCl) electrode were used as the counter and the reference electrodes, respectively. The same photoanodes were used as PV cells. In the aqueous electrolyte, 0.25 M Na_2S and 0.35 M Na_2SO_3 (pH 13) were utilized as hole scavengers. Sufficient N_2 bubbling was conducted for over 30 min before every measurement. The characteristics of PEC water splitting cells for hydrogen generation were measured using a custom-built cell.

2.4. Characterization. *2.4.1. Morphology and Energy Level of TiO_2.* A transmission electron microscope (TEM) JEM 2100 F (JEOL, Japan) was used with the ZrO/W(100) electron gun. The specific surface areas and pore size distributions of TiO_2 NPs were measured using Brunauer–Emmett–Teller (BET) and Barret–Joyner–Halenda (BJH) analyses with 3Flex (Micromeritics) using a N_2 carrier gas. The crystal phase of TiO_2 films coated on FTO substrates was measured by X-ray diffraction (XRD) using SmartLab (Rigaku) with Cu Kα radiation. Scanning electron microscope (SEM) images were measured using an FE-SEM (NOVA NANO SEM 450, FEI) at a 10.0 kV acceleration voltage and a field-free lens mode. To trace the energy level of TiO_2 films, UV–vis absorption spectroscopy (V-670 UV/vis spectrophotometer, Jasco) was used for TiO_2 without the scattering layer/FTO samples, and ultraviolet photoelectron spectroscopy (UPS, Thermo Fisher Scientific Co.) data were collected from a He I excitation source (21.2 eV). The UPS data were calibrated using the Fermi edge of Au. All samples for UPS were coated on a Si substrate.

2.4.2. Measurement of Time-Resolved Photoluminescence (TRPL). Time-resolved photoluminescence (TRPL) imaging was measured using an inverted-type scanning confocal microscope (MicroTime-200, Picoquant) with a 40× (air) objective at the Korea Basic Science Institute (KBSI) in Daegu Center (Republic of Korea). For an excitation source, a single-mode pulsed diode laser (470 nm with ~30 ps pulse width and ~10 μW laser power) was employed. The emission of each sample was collected using a single-photon avalanche diode (SPAD; PDM series, MPD). Using the time-tagged time-resolved (TTTR) data acquisition route, TRPL images (200 × 200 pixels) were recorded with 5 ms of the acquisition time for each pixel. Fittings of the PL decays were conducted by an exponential decay model using the following equation: $I(t) = \sum A_i e^{((-t)/\tau i)}$, where $I(t)$ is the time-dependent PL intensity, A is the amplitude, and τ is the PL lifetime.[42]

2.4.3. Measurement of the Current–Voltage (J–V) Curve and Incident Photon-to-Current Conversion Efficiencies (IPCEs). A Keithley (Model 2400) source meter and a solar simulator with a 300 W Xenon arc-lamp (Newport) were used for the measurement of the J–V characteristics of photoelectrochemical devices. The IPCEs of PV cells were measured using a QEX7 system (PV Measurements, Inc.). To avoid overestimating the power conversion efficiency (PCE) and the photocurrent density, masks (0.18 and 1.33 cm^2 active areas) were placed on the front side of the photoanodes.

2.4.4. Electrochemical Analyses. To estimate the density of surface states in the TiO_2 films with and without SPL, electrochemical methods of cyclic voltammetry (CV) and impedance spectroscopy (IS) were used with a three-electrode system and an aqueous electrolyte consisting of 0.25 M Na_2S and 0.35 M Na_2SO_3, which was the same composition used for PEC water splitting cells under dark conditions. Because of the basic pH of the electrolyte in the PEC water splitting cells (pH 13), a reversible hydrogen electrode (RHE) should be used as the reference electrode via correction of the Ag/AgCl reference electrode potential using the equation $V_{RHE} = V_{Ag/AgCl} + 0.197 + pH \times 0.059$.[43] The results of chemical capacitance (C_μ) and recombination resistance (R_{rec}) with the TiO_2/PbS-CdS QD photoanodes were extracted from IS measurements through the simplified equivalent circuit in the dark for PEC water splitting cells.[34] Different frequency ranges were applied in PV cells (1 MHz–10 mHz) and PEC water splitting cells (400 kHz–10 mHz) based on previous reports.[34,39] The film conductivity (σ) was directly calculated from the charge transport resistance (R_t) of the films, which was also analyzed by the IS measurements with the simplified equivalent circuit under dark conditions using the equation $\sigma = L/R_tA(1 - p_o)$, where L is the film thickness, A is the film area, and p_o is the film porosity.[44] The same quasi-Fermi levels in the TiO_2 films for both R_t and R_{rec} were used to obtain a correct η_{cc} at 1 sun illumination.[45] The equivalent conduction band potential (V_{ecb}) was used for the IS parameters (R_t and R_{rec}) and calculation of η_{cc}. Here, $V_{ecb} = V_F - \Delta E_c/q$, where V_F is the corrected Fermi voltage, which is the actual potential applied to the photoanode without the voltage drops from

https://dx.doi.org/10.1021/acsami.0c19352
ACS Appl. Mater. Interfaces 2021, 13, 6208–6218

the counter electrode and the series resistance from the applied potential, and ΔE_c is the shift in the CB with respect to the reference $E_{c,ref}$; $\Delta E_c = E_c - E_{c,ref}$.[46] For PV cells, IS has been frequently used to investigate the interfacial characteristics of charge accumulation, transport, and recombination using a diffusion−recombination equivalent circuit model.[47]

3. RESULTS AND DISCUSSION

3.1. Morphological and Structural Characteristics. Deposition of a surface passivation layer (SPL) by thermal hydrolysis of $TiCl_4$ led to clear morphological changes in mesoporous TiO_2 films, as shown in Figure S1a. Hereafter, mesoporous TiO_2 layers created with NPs having 20 and 30 nm particle diameters are referred to as T20 and T30, and the corresponding ones with SPLs are denoted as PT20 and PT30, respectively. An SPL whose thickness ranged from 2 to 5 nm was identified at the surface of the mesoporous TiO_2 films by TEM, high-resolution TEM (HR-TEM), and X-ray photoelectron spectroscopy (XPS) (Figures 2a and S1). In Figure 2a, the HR-TEM image of PT30 clearly indicates the effective growth of the SPL on the surface of TiO_2 NPs. The highly textured atomic structure represents the (101) plane of the anatase phase of the TiO_2 NP, and the corresponding *d*-spacing is 0.35 nm. On the top of the anatase surface, a distinct crystalline layer is formed with a comparable narrow *d*-spacing of 0.21−0.22 nm, attributed to the (003) plane of TiO_2(B). Interestingly, XRD patterns (Figures 2b and S2) of PT20 and PT30 showed a dual-phase (anatase and TiO_2(B)) nanocrystalline structure with polygonal plate- and needle-shaped crystallites, respectively, whereas only anatase crystals were obtained for T20 and T30 without the SPL (Figure S2). Here, a peak at $2\theta = 48.0°$ corresponds to the anatase in the (200) direction, and another peak at $2\theta = 43.5°$ (Figure 2b) is identified as the (003) plane of the polymorph TiO_2(B) structure.[48,49] Figure 2a also clearly shows the interplanar distance of the TiO_2(B) structure (0.21−0.22 nm) at the (003) plane, as confirmed by JCPDS no. 46-1237 in the SPL of PT30.[49] TEM and XRD data suggested that the SPL created a distinct crystal structure of the TiO_2(B) phase on the TiO_2 films, which resulted in morphological and structural changes and a corresponding change in electron transport properties. However, further analyses were not carried out to reveal the characteristics of TiO_2(B), such as a detailed growth mechanism and physical properties, since it was out of the scope of the current work.

Concerning the effects of the morphological changes on the SPL, BET and BJH data were found to correlate well with the SEM top-view images, indicating that there is a decrease in the pore size, pore volume, and surface area of the SPL (see Table 1 and Figures S3 and S4). For instance, the porosities (p_o) of 58 and 66% for T20 and T30 were reduced to 43 and 65% for PT20 and PT30, respectively.

The average coordination number of TiO_2 NPs (N), representing the average number of interconnections between TiO_2 per particle, is readily calculated using the equation $N = 3.08/p_o - 1.13$, with p_o being the porosity,[50] as listed in Table 1. N increased as the NP size decreased. Interestingly, the formation of the SPL notably resulted in an increase in N, particularly for PT20, suggesting a better architecture for electron transport.

PbS and CdS QDs were deposited on mesoporous TiO_2 films to prepare heterostructured photoanodes for TiO_2/PbS-CdS QDs by a SILAR method (see XRD and HR-TEM images of Figures S5 and S6). The deposition method is detailed in the Experimental Section. PbS and CdS QDs featuring particles 2−3 and 5−7 nm in diameter, respectively (Figure 2c and TEM and energy-dispersive X-ray spectrometry (EDX) images of Figure S7), were evenly distributed on the surface of TiO_2 films (Figure S8). The surface area of TiO_2 mesoporous films showed little difference after SPL deposition (Table 1), which would have a negligible influence on the surface coverage of QDs on TiO_2 films. Atomic ratios of PbS and CdS QDs on the TiO_2 films measured by XPS support the surface area results (Figure S9), suggesting that the surface fraction of deposited QDs on TiO_2 films with the SPL would be slightly lower than that of neat samples without the SPL.

Table 1. Results of Multipoint BET and BJH Analyses with N_2 Gas Adsorption and Desorption to Characterize the Surface Properties of Mesoporous TiO_2 Films with/without SPL

samples	surface area (m^2/g)	pore volume (cm^3/g)	pore size (nm)	[a]porosity (%)	coordination number
T20	90.66	0.35	15.41	58	4.21
PT20	84.60	0.20	9.27	43	5.99
T30	71.64	0.50	30.95	66	3.54
PT30	70.00	0.47	26.87	65	3.63

[a]Porosity (p_o) is calculated from the pore volume results using the equation $p_o = V_p/(1/\rho - V_p)$, where V_p is the cumulative specific pore volume and $1/\rho$ is the reciprocal of the density of TiO_2 (0.257 cm^3/g).[30]

3.2. Photoelectrochemical Performances of PV Cells and PEC Water Splitting Cells. The mesoporous TiO_2/PbS-CdS QD heterostructured photoanodes with/without the SPL were applied for both PV cells and PEC water splitting cells to evaluate their performances. A ZnS passivation layer was additionally deposited on the photoanodes to prevent photocorrosion and reduce recombination. Figure 3a depicts the device architectures of PV and PEC cells with mesoporous TiO_2/PbS-CdS QD heterostructured photoanodes.

The $J-V$ curves of PV cells with a 0.18 cm^2 active area of the photoanodes using the two-electrode sandwich devices at 1 sun conditions are shown in Figure 3b, and their corresponding photovoltaic parameters are summarized in Table 2. The IPCE and the integrated photocurrent density from the IPCE spectra support the $J-V$ results of PV cells (Figure 3c). The short-circuit current density (J_{sc}) significantly increased in the presence of the SPL (about 20%) compared to those of the references (T20 and T30), showing a J_{sc} higher than 25 mA/cm^2 (Table 2). In particular, PT20 showed a J_{sc} of 34.59 mA/cm^2 at 1 sun condition (Figure S11), which is the highest value reported in PV cells with TiO_2/QD photoanodes to date (Figure 1), whereas PT30 achieved the best PCE of PV cells (6.85%). The pore sizes of mesoporous TiO_2 films can account for the different PCEs observed in the samples. As shown in Table 1, the pore size of PT20 decreased to 9.27 nm after SPL deposition from the 15.41 nm of T20, increasing the likelihood of pore blockage when the QDs are deposited on mesoporous TiO_2 films. However, PT30 probably could maintain an adequate pore size to allow for electrolyte penetration even after the formation of the SPL. The small pore sizes of PT20 are also related to the large series resistance (R_s) in the film, directly resulting in a decreased FF and a consequent decrease in the PCE.

https://dx.doi.org/10.1021/acsami.0c19352
ACS Appl. Mater. Interfaces 2021, 13, 6208−6218

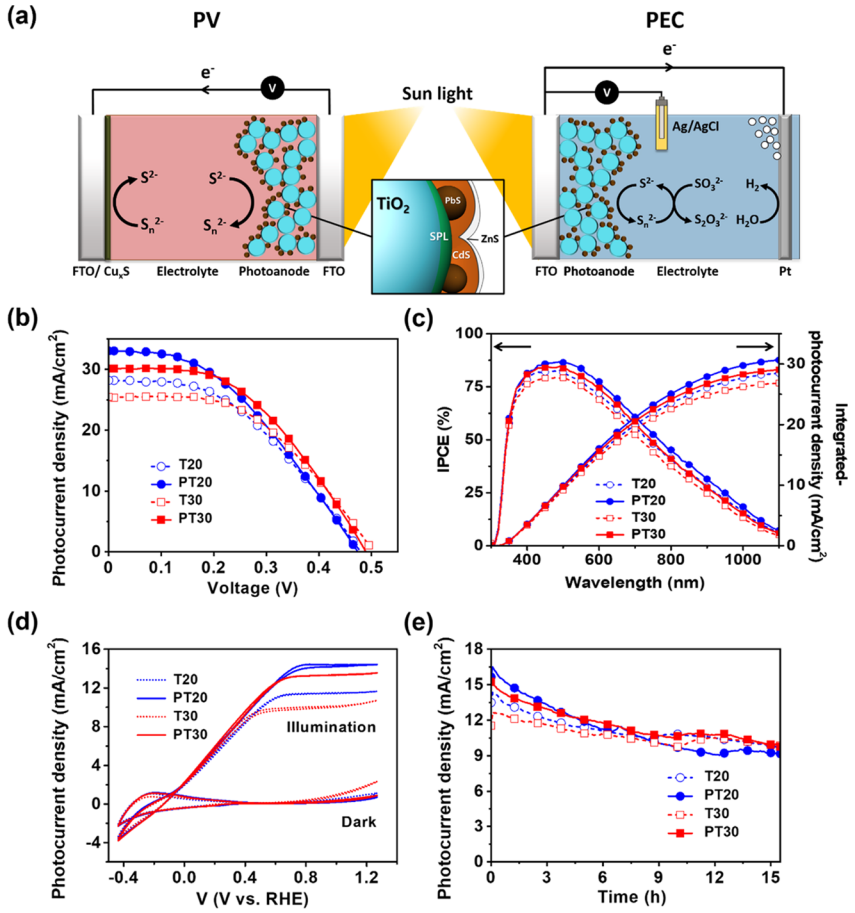

Figure 3. (a) Schematic illustrations of the structures and (b–e) performances of PV cells and PEC water splitting cells. The arrows in (a) indicate the charge transfer reactions between electrodes and electrolytes. Based on the same structure of both photoanodes for oxidizing sulfide (S^{2-}) to polysulfide (S_n^{2-}), Cu_xS CE regenerates the polysulfide at the PV cell, and the Pt CE reduces H_2 from H_2O at the PEC water splitting cell. (b) $J-V$ curves for PV cells, (c) IPCE and integrated J_{sc} for PV cells using two-electrode sandwich cells, (d) $J-V$ curves for PEC water splitting cells in the dark and under 1 sun conditions obtained by the three-electrode system with an Ag/AgCl reference electrode, and (e) chronoamperometric test for the long-term stability of PEC water splitting cells. All photocurrent densities were measured at 1 sun illumination. TiO_2/QD photoanodes of T20 (the blue empty circles and the dotted line), PT20 (the blue filled circles and the solid line), T30 (the red empty squares and the dotted line), and PT30 nm (the red filled squares and the solid line).

Table 2. Photovoltaic Characteristics of PV Cells with TiO_2 Films of Photoanodes for T20, PT20, T30, and PT30[a]

type of TiO_2	V_{oc} (V)	J_{sc} (mA/cm^2)	FF	PCE (%)
T20	0.48	28.36 ± 0.20	0.43	5.88 ± 0.03
PT20	0.47	33.67 ± 0.30	0.41	6.46 ± 0.02
T30	0.50	25.42 ± 0.25	0.49	6.19 ± 0.02
PT30	0.49	29.56 ± 0.49	0.47	6.83 ± 0.02

[a]The numbers indicate the average photovoltaic performances (J_{sc} and PEC) and standard deviations for five or six different cells (see Figure S10 for $J-V$ curves).

The outstanding photocurrents obtained for PV cells motivated us to use the photoanode in PEC water splitting cells for solar H_2 production. In comparison with PV cells, the performance of PEC water splitting photoanodes with a larger geometrical area (1.33 cm^2) showed similar trends (e.g., an increase in J_{sc} upon introduction of a SPL). Additionally, the photocurrent densities of PEC water splitting cells (J_{ph}) were higher than 10 mA/cm^2 at 0.82 V RHE for all samples, tested in a three-electrode arrangement (Figure 3d). Impressively, the highest J_{ph} of 14.4 mA/cm^2 at 0.82 V RHE was achieved with PT20. Note that the potential of 0.82 V RHE is based on all samples at a steady state. This is remarkable compared to previously reported values (see Table S1 for comparison). The steady-state, long-term stability of the photoanodes was tested (Figure 3e) at the same applied voltage (0.82 V RHE), showing relatively stable operation above 9 mA/cm^2 for more than 15 h under a strong alkaline condition (pH 13). H_2 generation was monitored by gas chromatography equipped with gas-enclosed PEC water splitting cells, and the corresponding current density profile was recorded at 1.4 V RHE under the same irradiation condition (1 sun) (a and b Figure S12b). The trend of H_2 generation was in excellent agreement with that of the photocurrent density in both PV cells and PEC water splitting cells. The faradic efficiency was also enhanced when the TiO_2 films were treated with a SPL (Figure S12c).

3.3. Effects of the SPL on Charge Injection Efficiency.

To gain further mechanistic insights into the operation of the photoelectrodes used, light-harvesting efficiency (η_{lh}), charge separation efficiency (η_{sp}), and charge collection efficiency (η_{cc}) were determined.[24] η_{sp} must be divided into charge injection and regeneration efficiencies (η_{inj} and η_{reg}, respectively), and η_{reg} is assumed to be unity for all cases since the regeneration rate of QDs by excess S^{2-} in the electrolyte is

https://dx.doi.org/10.1021/acsami.0c19352
ACS Appl. Mater. Interfaces 2021, 13, 6208–6218

nearly 3−4 orders of magnitude faster than the electron transfer rate from TiO_2 to oxidized QDs.[21,51]

Consequently, the effects of the SPL on η_{inj} were examined following the Marcus theory.[52] We considered the energy levels of TiO_2 films determining the reaction free energy for the injection rate (ΔG^0) from the CB of QDs (E_{c_QD}) to the CB of TiO_2 (E_{c_TiO2}) films: $\Delta G^0 = E_{c\_QD} - E_{c\_TiO_2}$. Based on the results of XRD and XPS for QDs (Figures S5 and S9), we assume that E_{c_QD} is the same in all samples. In other words, the relative ΔG^0 value is solely determined by $E_{c\_TiO_2}$. In this regard, we determined $E_{c\_TiO_2}$ first, as shown in Figure 4a,

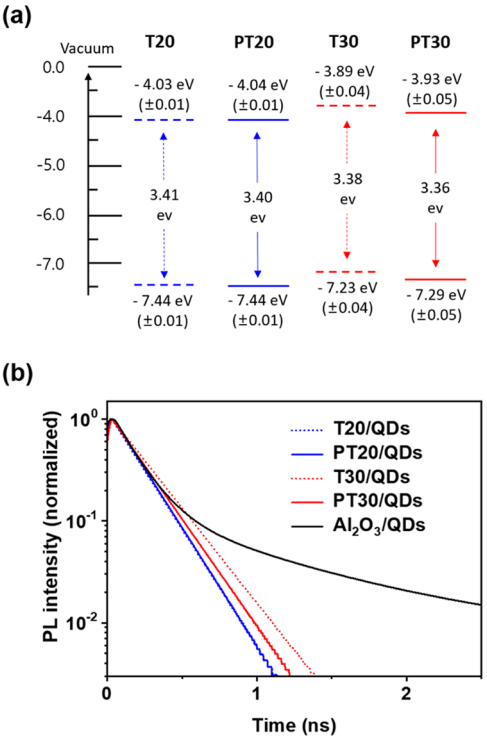

Figure 4. (a) Energy levels of TiO_2 films obtained from the spectroscopic data of T20 and T30 and of PT20 and PT30. (b) TRPL emission decay spectra of TiO_2/PbS-CdS QD heterostructured photoanodes measured at 500 nm. The Al_2O_3/QD film (black line) was used as the control electrode.

using the Tauc plots from UV−vis absorption spectra and UPS valence band (VB) spectra (Figure S13). These results suggest that the SPL slightly decreases the optical band gap (E_g) of TiO_2 films along with the CB energy level. PT20 (E_g = 3.40 eV) showed little difference from T20 (3.41 eV) in terms of band gap, while PT30 showed a larger change in the CB. The results also showed that ΔG^0 increased in the following order: T30 < PT30 < T20 ∼ PT20.

Figure 4b shows the emission decay spectra of TRPL for QDs on TiO_2 and QDs on Al_2O_3 as a reference, from which all electron injection parameters can be obtained.[53] Table 3 lists the electron injection parameters of PL lifetime (τ_{PL}), electron injection rate constant (k_{inj}), and electron injection efficiency (η_{inj}). The results confirm that both k_{inj} and η_{inj} are consistent with ΔG^0 in all TiO_2/QD heterostructured photoanodes, suggesting their strong correlation. Even though a change in η_{inj} was observed, it was very small. This is different from the large increase in η_{inj} typically observed when an SPL was introduced by $TiCl_4$ treatment in TiO_2/dye photoanodes.[24]

Table 3. Calculated PL Lifetime (τ_{PL}), Electron Injection Rate Constant (k_{inj}), and Electron Injection Efficiency (η_{inj}) by the TRPL Emission Decay Spectra of TiO_2/PbS-CdS QD Heterostructured Photoanodes[a]

photoanode semiconductors	τ_{PL} (ns)	[b]k_{inj} (10^9/s)	[c]η_{inj} (%)
T20	0.189	5.11	96.62
PT20	0.188	5.14	96.64
T30	0.232	4.13	95.86
PT30	0.207	4.65	96.30
Al_2O_3	5.601		

[a]Al_2O_3/QDs were used for the control cell. [b]τ_{PL} was calculated from the rate for electron injection by $k_{inj} = 1/\tau_{titania} - 1/\tau_{alumina}$, where $\tau_{titania}$ and $\tau_{alumina}$ are the emission lifetimes of TiO_2/QDs and Al_2O_3/QDs as the control cell, respectively.[42] [c]η_{inj} was estimated through $\eta_{inj} = k_{inj}/(k_{inj} + k_{non})$, where k_{non} is the noninjection rate constant, and $k_{non} = 1/\tau_{alumina}$.[42]

Therefore, the reason for the above results is more likely due to electron injection from PbS QDs to the TiO_2 film in the ultrafast range of femtoseconds.[54]

3.4. Increases in the Surface State Concentration and the Charge Collection Efficiency. It is well-known that surface states modified by the presence of an SPL play a key role in the energetic and kinetic properties for charge transport and transfer reactions, which are directly related to η_{cc}.[34] To estimate the density of surface states in the TiO_2 films, chemical capacitance (C_μ) was measured by cyclic voltammetry (CV) and electrochemical impedance spectroscopy (IS) in a PEC cell (Figure S14). Figure 5a shows the density of trap states (DOS) estimated from the C_μ of TiO_2 films as a function of applied potential. The DOS peaks at 0−0.2 V RHE showed Gaussian behavior (marked as the yellow area in Figure 5a), which has been interpreted as a reversible filling of surface states located in traps below the CB of TiO_2.[34,35,55] The DOS increased after the deposition of the SPL (PT20 and PT30), suggesting that this layer increased the density of surface states on the TiO_2 films.

The impact of the SPL on the energy distribution of TiO_2 films directly correlates to the change of the chemical diffusion coefficient (D_n). When a diffusion coefficient depends on E_F, it is referred to as the "chemical" diffusion coefficient.[31,53,56] Mesoporous nanostructured semiconductors featured charge transport within a broad distribution of localized states. Consequently, the change in electrochemical potential (Fermi energy level, E_F) of charges modified the occupation of localized states, impacting their diffusion. Therefore, D_n can be affected by both the energy distributions of nanostructured semiconductors and morphology. Figure 5b shows D_n as a function of applied potential for TiO_2 films. D_n of all samples increased with negative potential, indicating that the transport mechanism follows the multiple trapping/detrapping transport model.[56] Interestingly, D_n exhibited the same trends as DOS and increased as T30 < T20 < PT30 < PT20 in the potential range of 0−0.1 V RHE. These results provide strong evidence that the surface states in the TiO_2 film introduced by the SPL have a direct correlation with D_n. Since the energy level of the surface states of the TiO_2 films is located at the effective range of conduction (about 0.5−1.0 eV below the CB),[56] we conclude that D_n increases due to the increase in the density of surface states.

On the other hand, morphological changes such as porosity (p_o), coordination number (N), and particle size induced by

https://dx.doi.org/10.1021/acsami.0c19352
ACS Appl. Mater. Interfaces 2021, 13, 6208−6218

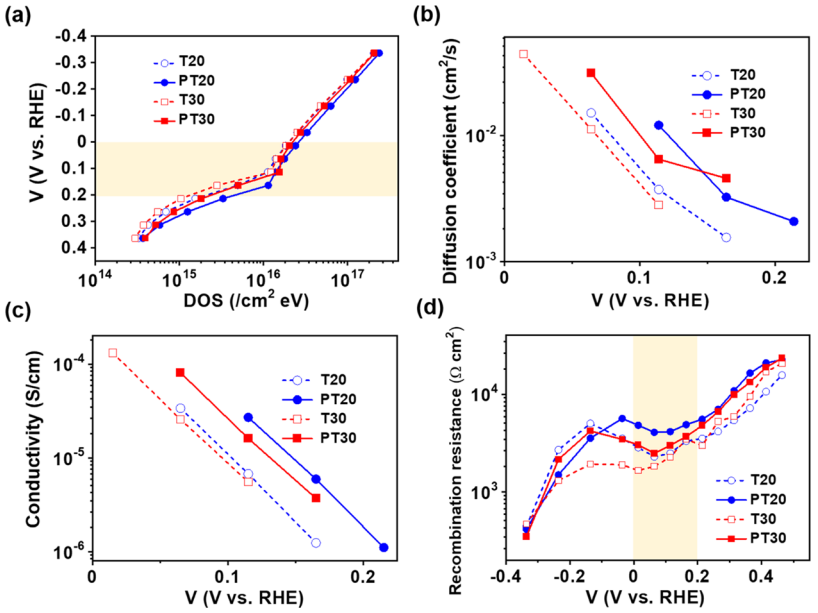

Figure 5. Several electrochemical parameters for charge accumulation and transport properties in the TiO_2 films. (a) Calculated DOS of TiO_2 films in the dark as a function of potential from chemical capacitance (C_μ) below the CB. The yellow marked potential region indicates the peaks at 0–0.2 V, supporting the presence of surface states. (b) Chemical diffusion coefficient (D_n), (c) electron conductivity (σ) calculated by charge transport resistance (R_t) of the TiO_2 films in the dark, and potentials for (b) and (c) are marked in yellow in (a). (d) Recombination resistance (R_{rec}) of PEC water splitting cells with TiO_2/PbS-CdS QD heterostructured photoanodes as a function of potential in the dark. The IS measurements were used to extract the parameters with the simplified equivalent circuit for transport, chemical capacitance, and charge transfer using a three-electrode system. T20 (blue empty circles), PT20 (blue filled circles), T30 (red empty squares), and PT30 nm (red filled squares).

the SPL can also affect the intrinsic diffusion properties of TiO_2 films. As expected, D_n increases with an increase in N and a decrease in p_o during SPL formation.[57] Regarding the particle size effect, we expected that the small TiO_2 NPs would have a low D_n primarily due to the increased grain boundary area.[30] However, Figure 5b shows that the small TiO_2 NPs have a high D_n instead. Therefore, we conclude that both p_o and N have a stronger influence on D_n compared to the particle size. In any case, surface states and particle sizes may be related.[58]

Based on the multiple trapping/detrapping transport model for charge transport in mesoporous nanostructured semiconductors and the generalized Einstein relation, conductivity (σ) can be expressed by the following equation

$$\sigma = C_\mu^{trap} D_n(E_F) \quad (1)$$

Here, C_μ^{trap} is the trap state capacitance, and $D_n(E_F)$ is the electron diffusion coefficient.[53]

If the density of trap states can produce localized electrons, the DOS in the band gap is associated with the trap state capacitance. Therefore, the energetic distribution of the density of trap states (DOS = $g(E_F)$) can be calculated by the equation $C_\mu^{trap}(E) = qg(E_F)$, where q is the elemental charge.[35,47] Clearly, the SPL increased the conductivity of TiO_2 films through an increase in the density of surface states and morphological changes in the TiO_2 film (Figure 5c).

Electron recombination is another important factor affected by the SPL via the density of surface states, significantly influencing charge collection. Figure 5d shows the evolution of recombination resistance (R_{rec}) of heterostructured TiO_2/PbS-CdS photoanodes with the applied potential. This resistance increased with the anodic (positive) potential. The valley at 0–0.2 eV is related to recombination through surface states.[34] Interestingly, although the density of surface states was increased by the SPL, it efficiently blocked electron recombination. Furthermore, R_{rec} and σ followed similar trends and were increased by the SPL. The decreased dark currents in Figure 3d treated with the SPL supported well the recombination blocking effect of the SPL.

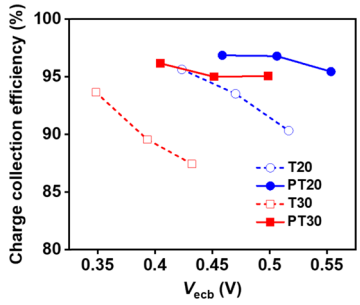

Figure 6. Charge collection efficiency (η_{cc}) of PV cells with TiO_2/PbS-CdS QD heterostructured photoanodes with T20 (blue empty circles), PT20 (blue filled circles), T30 (red empty squares), and PT30 nm (red filled squares) at 1 sun condition. Values were calculated using the results of R_t and R_{rec} as a function of V_{ecb} in PV cells (Figure S15).

Both conductivity and recombination through the TiO_2 films ultimately influence the charge collection efficiency, η_{cc}, which in turn directly controlled the photocurrent densities (J_{sc} and J_{ph}) of the photoelectrochemical devices. η_{cc} can be estimated by the equation

$$\eta_{cc} = 1 - R_t/R_{rec} \quad (2)$$

where R_t is the transport resistance.[45,59]

Figure S15 shows the results of R_t and R_{rec} as a function of the equivalent conduction band potential, V_{ecb}, in PV cells extracted from the IS measurements. Here, V_{ecb} can be

https://dx.doi.org/10.1021/acsami.0c19352
ACS Appl. Mater. Interfaces 2021, 13, 6208–6218

obtained from $V_{ecb} = V_F - \Delta E_c/q$ to compare the recombination resistance (R_{rec}), where V_F is the corrected Fermi voltage excluding the influences of series resistance and the CE in the device and ΔE_c is the shift in the CB with respect to the reference $E_{c,ref}$; $\Delta E_c = E_c - E_{c,ref}$.[46] The calculated η_{cc} shown in Figure 6 increases with nearly the same trend as the conductivity and recombination resistance of the TiO_2 films and the photocurrent densities of TiO_2/PbS-CdS QD heterostructured photoanodes in both PV cells and PEC water splitting cells. Comparing the parameters for photocurrent densities such as the η_{lh} calculated via IPCE in Table S2, η_{cc}, and η_{inj} values, we demonstrated that η_{cc} controls the photocurrent densities of PV cells with the TiO_2 films. Consequently, high photocurrent densities greater than 30 mA/cm^2 for PV cells with SPL samples (PT20 and PT30) were obtained primarily due to the enhancement of film conductivity, as well as the decrease in recombination kinetics induced by the SPL.

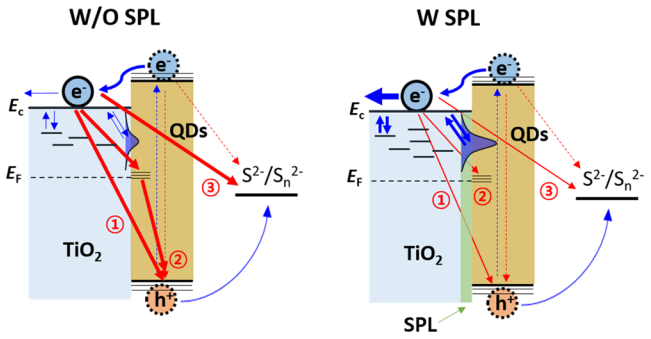

Figure 7. Schematic illustration of the effects of the SPL on the kinetics of the TiO_2/QD heterostructured photoanode with the S^{2-}/S_n^{2-} electrolyte. The left and right sides indicate without (W/O) and with (W) an SPL, respectively. The blue arrows represent the charge flow pathway for the current and the red arrows represent recombination pathways of electrons under illumination.

Figure 7 summarizes the effects of the SPL on the photocurrent density of the TiO_2/QD heterostructured photoanode.

- After light absorption of QDs, neither charge injection nor regeneration of oxidized QDs was significantly affected by the SPL. This may be partly related to the ultrafast electron injection rate of QDs caused by the direct deposition method.[54]
- The increased density of surface states induced by the SPL facilitated multiple trapping transport, which was demonstrated by the improvement of the chemical diffusion coefficient. The facilitated multiple trapping/detrapping transport along with morphological changes of the mesoporous TiO_2 films (related to increased N) increased the electron conductivity of TiO_2 films.
- Due to the different energy levels of CdS and PbS QDs, the electrons at the CB of TiO_2 without an SPL can have multiple pathways for electron recombination through the TiO_2/QD and TiO_2/electrolyte interfaces such as (1) electron transfer to the long-lived holes at the VB of QDs, (2) QD trap-mediated electron transfer, and (3) electron transfer to the electrolyte. We demonstrated that the SPL can play a key role in decreasing the recombination kinetics at the TiO_2/QD and TiO_2/electrolyte interfaces. However, to confirm directly the effects of the SPL on (1) and (2), further experiments are required.

Since both η_{inj} and η_{lh} are almost unity at the TiO_2/QD heterostructured photoanode, maximizing the photocurrent density by improving η_{cc} can be an effective strategy. A higher photocurrent density can be obtained by incorporating an SPL despite the slight loss of η_{lh} due to the decreased surface area (Table S2). As a result, the introduction of a SPL is a viable strategy to maximize η_{cc} and to optimize the photocurrent density by enhancing conductivity and blocking recombination at the TiO_2/QD heterostructured photoanode.

4. CONCLUSIONS

We investigated the effect of a TiO_2 SPL deposited on a mesoporous TiO_2 film surface for TiO_2/PbS-CdS QD heterostructured photoanodes for PV and water splitting PEC devices. Such a TiO_2 SPL increased the density of surface states and also the coordination number of the TiO_2 NPs, both leading to an increase in electron conductivity through the TiO_2 film. The increase in electron conductivity in the TiO_2 film is mostly due to the improvement of the chemical diffusion coefficient according to the multiple trapping/detrapping transport model. Concomitantly, the reduction of back electron transfers, known to be the conventional role of SPLs, also helps to increase η_{cc} in the TiO_2 films. Therefore, the TiO_2/PbS-CdS QD photoanodes showed a J_{sc} of 34.59 mA/cm^2 in PV cells and a photocurrent density of 14.43 mA/cm^2 at 0.82 V RHE in PEC water splitting cells. On the other hand, η_{inj}, which mainly affects the photocurrent density in photoanodes, was not significantly different for devices with/without SPLs. The results could provide new directions and important milestones for the development of high-performance PEC devices with TiO_2/QD heterostructured photoanodes.

■ ASSOCIATED CONTENT

Supporting Information

The Supporting Information is available free of charge at https://pubs.acs.org/doi/10.1021/acsami.0c19352.

TEM, XPS, XRD, BET, BJH, SEM, EDX, and conformal images of fluorescence lifetime for morphology and structure characteristics; J–V curve; IPCE of the PV cell for PEC performances; hydrogen generation amounts and faradic efficiency of PEC water splitting cells; UPS and UV–vis absorption spectra for energy levels of samples; electrochemical analysis results for surface states and charge collection; and previous reported PEC performances of metal oxide/QD heterostructured photoanodes for hydrogen generation and calculated light-harvesting efficiency (PDF)

■ AUTHOR INFORMATION

Corresponding Authors

Jin Ho Bang − *Department of Chemical and Molecular Engineering and Department of Applied Chemistry, Center for Bionano Intelligence Education and Research, Hanyang University, Ansan 15588, Gyeonggi-do, Korea;* orcid.org/0000-0002-6717-3454; Email: jbang@hanyang.ac.kr

Sixto Giménez − *Institute of Advanced Materials (INAM), Universitat Jaume I, Castelló 12006, Spain;* orcid.org/0000-0002-4522-3174; Email: sjulia@uji.es

https://dx.doi.org/10.1021/acsami.0c19352
ACS Appl. Mater. Interfaces 2021, 13, 6208−6218

Yong Soo Kang − *Department of Energy Engineering and Center for Next Generation Dye-Sensitized Solar Cells, Hanyang University, Seoul 04763, Korea;* orcid.org/0000-0003-4989-321X; Email: kangys@hanyang.ac.kr

Authors

Tea-Yon Kim − *Department of Chemistry, Michigan State University, East Lansing, Michigan 48824-1322, United States;* orcid.org/0000-0001-8510-8261

Byung Su Kim − *Department of Energy Engineering and Center for Next Generation Dye-Sensitized Solar Cells, Hanyang University, Seoul 04763, Korea*

Jong Gyu Oh − *Department of Energy Engineering, Hanyang University, Seoul 04763, Korea*

Seul Chan Park − *Department of Energy Engineering and Center for Next Generation Dye-Sensitized Solar Cells, Hanyang University, Seoul 04763, Korea*

Jaeyoung Jang − *Department of Energy Engineering, Hanyang University, Seoul 04763, Korea;* orcid.org/0000-0002-5548-8563

Thomas W. Hamann − *Department of Chemistry, Michigan State University, East Lansing, Michigan 48824-1322, United States;* orcid.org/0000-0001-6917-7494

Young Soo Kang − *Korea Center for Artificial Photosynthesis and Department of Chemistry, Sogang University, Seoul 04107, Korea;* orcid.org/0000-0001-5746-8171

Complete contact information is available at: https://pubs.acs.org/10.1021/acsami.0c19352

Author Contributions

$^{\nabla}$T.-Y.K. and B.S.K. contributed equally to this work.

Notes

The authors declare no competing financial interest.

■ ACKNOWLEDGMENTS

This work was supported by the Korea Center for Artificial Photosynthesis (KCAP) of Sogang University, funded by the Ministry of Science, ICT, and Future Planning (MSIP) through a National Research Foundation of Korea (Grant no. 2009-0093883). This work also was supported by a grant from the Basic Science Research Program through the National Research Foundation (NRF) of Korea funded by the Ministry of Science and ICT (NRF-2019R1A2C1003429) and by the Ministry of Education (NRF-2018R1A6A1A03024231). Also, this work was supported by the Ministerio de Ciencia, Innovacio´n y Universidades of Spain through the project ENE2017−85087-C3-1-R. Therefore, the authors acknowledge and thank the Korean and Spanish governments for technical and financial support. S. D. G.

■ REFERENCES

(1) Nozik, A. J. Quantum Dot Solar Cells. *Phys. E* **2002**, *14*, 115−120.
(2) Kamat, P. V. Quantum Dot Solar Cells. Semiconductor Nanocrystals as Light Harvesters. *J. Phys. Chem. C* **2008**, *112*, 18737−18753.
(3) de Mello Donegá, C. Synthesis and Properties of Colloidal Heteronanocrystals. *Chem. Soc. Rev.* **2011**, *40*, 1512−1546.
(4) Alivisatos, A. P. Semiconductor Clusters, Nanocrystals, and Quantum Dots. *Science* **1996**, *271*, 933−937.
(5) Kramer, I. J.; Sargent, E. H. The Architecture of Colloidal Quantum Dot Solar Cells: Materials to Devices. *Chem. Rev.* **2014**, *114*, 863−882.
(6) Wang, K.; Tong, X.; Zhou, Y.; Zhang, H.; Navarro-Pardo, F.; Selopal, G. S.; Liu, G.; Tang, J.; Wang, Y.; Sun, S.; Ma, D.; Zhiming, M. W.; Vidal, F.; Zhao, H.; Sun, X.; Rosei, F. Efficient Solar-Driven Hydrogen Generation Using Colloidal Heterostructured Quantum Dots. *J. Mater. Chem. A* **2019**, *7*, 14079−14088.
(7) Selopal, G. S.; Zhao, H.; Wang, Z. M.; Rosei, F. Core/Shell Quantum Dots Solar Cells. *Adv. Funct. Mater.* **2020**, *30*, No. 1908762.
(8) Liu, J.; Zhang, H.; Navarro-Pardo, F.; Selopal, G. S.; Sun, S.; Wang, Z. M.; Zhao, H.; Rosei, F. Hybrid Surface Passivation of PbS/CdS Quantum Dots for Efficient Photoelectrochemical Hydrogen Generation. *Appl. Surf. Sci.* **2020**, *530*, No. 147252.
(9) Fan, J. Z.; Vafaie, M.; Bertens, K.; Sytnyk, M.; Pina, J. M.; Sagar, L. K.; Ouellette, O.; Proppe, A. H.; Rasouli, A. S.; Gao, Y.; Baek, S.-W.; Chen, B.; Laquai, F.; Hoogland, S.; García de Arquer, F. P.; Heiss, W.; Sargent, E. H. Micron Thick Colloidal Quantum Dot Solids. *Nano Lett.* **2020**, *20*, 5284−5291.
(10) Chandiran, A. K.; Abdi-Jalebi, M.; Nazeeruddin, M. K.; Grätzel, M. Analysis of Electron Transfer Properties of ZnO and TiO_2 Photoanodes for Dye-Sensitized Solar Cells. *ACS Nano* **2014**, *8*, 2261−2268.
(11) Lee, J.-W.; Son, D.-Y.; Ahn, T. K.; Shin, H.-W.; Kim, I. Y.; Hwang, S.-J.; Ko, M. J.; Sul, S.; Han, H.; Park, N.-G. Quantum-Dot-Sensitized Solar Cell with Unprecedentedly High Photocurrent. *Sci. Rep.* **2013**, *3*, No. 1050.
(12) Wang, H.; Kubo, T.; Nakazaki, J.; Kinoshita, T.; Segawa, H. PbS-Quantum-Dot-Based Heterojunction Solar Cells Utilizing ZnO Nanowires for High External Quantum Efficiency in the Near-Infrared Region. *J. Phys. Chem. Lett.* **2013**, *4*, 2455−2460.
(13) Abbas, M. A.; Basit, M. A.; Park, T. J.; Bang, J. H. Enhanced Performance of PbS-Sensitized Solar Cells via Controlled Successive Ionic-Layer adsorption and Reaction. *Phys. Chem. Chem. Phys.* **2015**, *17*, 9752−9760.
(14) Hou, B.; Cho, Y.; Kim, B. S.; Hong, J.; Park, J. B.; Ahn, S. J.; Sohn, J. I.; Cha, S.; Kim, J. M. Highly Monodispersed PbS Quantum Dots for Outstanding Cascaded-Junction Solar Cells. *ACS Energy Lett.* **2016**, *1*, 834−839.
(15) Bi, Y.; Pradhan, S.; Gupta, S.; Akgul, M. Z.; Stavrinadis, A.; Konstantatos, G. Infrared Solution-Processed Quantum Dot Solar Cells Reaching External Quantum Efficiency of 80% at 1.35 μm and Jsc in Excess of 34 mA cm^{-2}. *Adv. Mater.* **2018**, *30*, No. 1704928.
(16) Kim, J.; Ouellette, O.; Voznyy, O.; Wei, M.; Choi, J.; Choi, M.-J.; Jo, J. W.; Baek, S.-W.; Fan, J.; Saidaminov, M. I.; Sun, B.; Li, P.; Nam, D.-H.; Hoogland, S.; Lu, Z.-H.; García de Arquer, F. P.; Sargent, E. H. Butylamine-Catalyzed Synthesis of Nanocrystal Inks Enables Efficient Infrared CQD Solar Cells. *Adv. Mater.* **2018**, *30*, No. 1803830.
(17) Xia, Y.; Liu, S.; Wang, K.; Yang, X.; Lian, L.; Zhang, Z.; He, J.; Liang, G.; Wang, S.; Tan, M.; Song, H.; Zhang, D.; Gao, J.; Tang, J.; Beard, M. C.; Zhang, J. Cation-Exchange Synthesis of Highly Monodisperse PbS Quantum Dots from ZnS Nanorods for Efficient Infrared Solar Cells. *Adv. Funct. Mater.* **2020**, *30*, No. 1907379.
(18) Li, X.-B.; Tung, C.-H.; Wu, L.-Z. Semiconducting Quantum Dots for Artificial Photosynthesis. *Nat. Rev. Chem.* **2018**, *2*, 160−173.
(19) Hamann, T. W. Perovskites Take Lead in Solar Hydrogen Race. *Science* **2014**, *345*, 1566−1567.
(20) Liu, M.; Nam, C.-Y.; Black, C. T.; Kamcev, J.; Zhang, L. Enhancing Water Splitting Activity and Chemical Stability of Zinc Oxide Nanowire Photoanodes with Ultrathin Titania Shells. *J. Phys. Chem. C* **2013**, *117*, 13396−13402.
(21) Hodes, G. Comparison of Dye- and Semiconductor-Sensitized Porous Nanocrystalline Liquid Junction Solar Cells. *J. Phys. Chem. C* **2008**, *112*, 17778−17787.
(22) Bai, Y.; Mora-Seró, I.; De Angelis, F.; Bisquert, J.; Wang, P. Titanium Dioxide Nanomaterials for Photovoltaic Applications. *Chem. Rev.* **2014**, *114*, 10095−10130.
(23) Basit, M. A.; Abbas, M. A.; Jung, E. S.; Park, Y. M.; Bang, J. H.; Park, T. J. Strategic PbS Quantum Dot-Based Multilayered Photoanodes for High Efficiency Quantum Dot-Sensitized Solar Cells. *Electrochim. Acta* **2016**, *211*, 644−651.

(24) O'Regan, B. C.; Durrant, J. R.; Sommeling, P. M.; Bakker, N. J. Influence of the $TiCl_4$ Treatment on Nanocrystalline TiO2 Films in Dye-Sensitized Solar Cells. 2. Charge Density, Band Edge Shifts, and Quantification of Recombination Losses at Short Circuit. *J. Phys. Chem. C* **2007**, *111*, 14001−14010.
(25) Barnes, P. R. F.; Anderson, A. Y.; Koops, S. E.; Durrant, J. R.; O'Regan, B. C. Electron Injection Efficiency and Diffusion Length in Dye-Sensitized Solar Cells Derived from Incident Photon Conversion Efficiency Measurements. *J. Phys. Chem. C* **2009**, *113*, 1126−1136.
(26) Leng, W. H.; Barnes, P. R. F.; Juozapavicius, M.; O'Regan, B. C.; Durrant, J. R. Electron Diffusion Length in Mesoporous Nanocrystalline TiO_2 Photoelectrodes during Water Oxidation. *J. Phys. Chem. Lett.* **2010**, *1*, 967−972.
(27) Sommeling, P. M.; O'Regan, B. C.; Haswell, R. R.; Smit, H. J. P.; Bakker, N. J.; Smits, J. J. T.; Kroon, J. M.; van Roosmalen, J. A. M. Influence of a $TiCl_4$ Post-Treatment on Nanocrystalline TiO_2 Films in Dye-Sensitized Solar Cells. *J. Phys. Chem. B* **2006**, *110*, 19191−19197.
(28) Lee, S.-W.; Ahn, K.-S.; Zhu, K.; Neale, N. R.; Frank, A. J. Effects of $TiCl_4$ Treatment of Nanoporous TiO_2 Films on Morphology, Light Harvesting, and Charge-Carrier Dynamics in Dye-Sensitized Solar Cells. *J. Phys. Chem. C* **2012**, *116*, 21285−21290.
(29) Mora-Seró, I.; Giménez, S.; Fabregat-Santiago, F.; Gómez, R.; Shen, Q.; Toyoda, T.; Bisquert, J. Recombination in Quantum Dot Sensitized Solar Cells. *Acc. Chem. Res.* **2009**, *42*, 1848−1857.
(30) Park, K.; Zhang, Q.; Myers, D.; Cao, G. Charge Transport Properties in TiO_2 Network with Different Particle Sizes for Dye Sensitized Solar Cells. *ACS Appl. Mater. Interfaces* **2013**, *5*, 1044−1052.
(31) Bisquert, J. Interpretation of Electron Diffusion Coefficient in Organic and Inorganic Semiconductors with Broad Distributions of States. *Phys. Chem. Chem. Phys.* **2008**, *10*, 3175−3194.
(32) Peter, L. M. Photoelectrochemistry: From Basic Principles to Photocatalysis. In *Photocatalysis: Fundamentals and Perspectives*; The Royal Society of Chemistry: Cambridge, U.K, 2016; Chapter 1, pp 1−28.
(33) Nunzi, F.; Mosconi, E.; Storchi, L.; Ronca, E.; Selloni, A.; Grätzel, M.; De Angelis, F. Inherent Electronic Trap States in TiO_2 Nanocrystals: Effect of Saturation and Sintering. *Energy Environ. Sci.* **2013**, *6*, 1221−1229.
(34) Gimenez, S.; Dunn, H. K.; Rodenas, P.; Fabregat-Santiago, F.; Miralles, S. G.; Barea, E. M.; Trevisan, R.; Guerrero, A.; Bisquert, J. Carrier Density and Interfacial Kinetics of Mesoporous TiO_2 in Aqueous Electrolyte Determined by Impedance Spectroscopy. *J. Electroanal. Chem.* **2012**, *668*, 119−125.
(35) Klahr, B.; Gimenez, S.; Fabregat-Santiago, F.; Hamann, T.; Bisquert, J. Water Oxidation at Hematite Photoelectrodes: The Role of Surface States. *J. Am. Chem. Soc.* **2012**, *134*, 4294−4302.
(36) Wang, H.; He, J.; Boschloo, G.; Lindström, H.; Hagfeldt, A.; Lindquist, S.-E. Electrochemical Investigation of Traps in a Nanostructured TiO_2 Film. *J. Phys. Chem. B* **2001**, *105*, 2529−2533.
(37) Abdi-Jalebi, M.; Dar, M. I.; Sadhanala, A.; Senanayak, S. P.; Giordano, F.; Zakeeruddin, S. M.; Grätzel, M.; Friend, R. H. Impact of a Mesoporous Titania−Perovskite Interface on the Performance of Hybrid Organic−Inorganic Perovskite Solar Cells. *J. Phys. Chem. Lett.* **2016**, *7*, 3264−3269.
(38) Ito, S.; Murakami, T. N.; Comte, P.; Liska, P.; Grätzel, C.; Nazeeruddin, M. K.; Grätzel, M. Fabrication of Thin Film Dye Sensitized Solar Cells with Solar to Electric Power Conversion Efficiency over 10%. *Thin Solid Films* **2008**, *516*, 4613−4619.
(39) Kim, T.-Y.; Lee, T. K.; Kim, B. S.; Park, S. C.; Lee, S.; Im, S. S.; Bisquert, J.; Kang, Y. S. Triumphing over Charge Transfer Limitations of PEDOT Nanofiber Reduction Catalyst by 1,2-Ethanedithiol Doping for Quantum Dot Solar Cells. *ACS Appl. Mater. Interfaces* **2017**, *9*, 1877−1884.
(40) Kim, C. S.; Choi, S. H.; Bang, J. H. New Insight into Copper Sulfide Electrocatalysts for Quantum Dot-Sensitized Solar Cells: Composition-Dependent Electrocatalytic Activity and Stability. *ACS Appl. Mater. Interfaces* **2014**, *6*, 22078−22087.
(41) Choi, H. M.; Ji, I. A.; Bang, J. H. Metal Selenides as a New Class of Electrocatalysts for Quantum Dot-Sensitized Solar Cells: A Tale of $Cu_{1.8}Se$ and PbSe. *ACS Appl. Mater. Interfaces* **2014**, *6*, 2335−2343.
(42) Kim, T.-Y.; Lee, S.; Jeong, D.; Lee, T. K.; Kim, B. S.; Chae, I. S.; Kang, Y. S. Poly(3,4-ethylenedioxythiophene) Quantum Dot-Sensitized Solar Cells in the Solid-State Utilizing Polymer Electrolyte. *ACS Appl. Energy Mater.* **2018**, *1*, 290−295.
(43) Rodenas, P.; Song, T.; Sudhagar, P.; Marzari, G.; Han, H.; Badia-Bou, L.; Gimenez, S.; Fabregat-Santiago, F.; Mora-Sero, I.; Bisquert, J.; Paik, U.; Kang, Y. S. Quantum Dot Based Heterostructures for Unassisted Photoelectrochemical Hydrogen Generation. *Adv. Energy Mater.* **2013**, *3*, 176−182.
(44) Herraiz-Cardona, I.; Fabregat-Santiago, F.; Renaud, A.; Julián-López, B.; Odobel, F.; Cario, L.; Jobic, S.; Giménez, S. Hole Conductivity and Acceptor Density of P-Type $CuGaO_2$ Nanoparticles Determined by Impedance Spectroscopy: The Effect of Mg Doping. *Electrochim. Acta* **2013**, *113*, 570−574.
(45) Hagfeldt, A.; Boschloo, G.; Sun, L.; Kloo, L.; Pettersson, H. Dye-Sensitized Solar Cells. *Chem. Rev.* **2010**, *110*, 6595−6663.
(46) Kim, T.-Y.; Song, D.; Barea, E. M.; Lee, J. H.; Kim, Y. R.; Cho, W.; Lee, S.; Rahman, M. M.; Bisquert, J.; Kang, Y. S. Origin of High Open-Circuit Voltage in Solid State Dye-Sensitized Solar Cells Employing Polymer Electrolyte. *Nano Energy* **2016**, *28*, 455−461.
(47) Fabregat-Santiago, F.; Garcia-Belmonte, G.; Mora-Seró, I.; Bisquert, J. Characterization of Canostructured Hybrid and Organic Solar Cells by Impedance Spectroscopy. *Phys. Chem. Chem. Phys.* **2011**, *13*, 9083−9118.
(48) Chimupala, Y.; Hyett, G.; Simpson, R.; Mitchell, R.; Douthwaite, R.; Milne, S. J.; Brydson, R. D. Synthesis and Characterization of Mixed Phase Anatase TiO_2 and Sodium-Doped TiO_2(B) Thin Films by Low Pressure Chemical Vapour Deposition (LPCVD). *RSC Adv.* **2014**, *4*, 48507−48515.
(49) Sun, C.; Xu, Q.; Xie, Y.; Ling, Y.; Hou, Y. Designed Synthesis of Anatase−TiO_2(B) Biphase Nanowire/ZnO Nanoparticle Heterojunction for Enhanced Photocatalysis. *J. Mater. Chem. A* **2018**, *6*, 8289−8298.
(50) van de Lagemaat, J.; Benkstein, K. D.; Frank, A. J. Relation between Particle Coordination Number and Porosity in Nanoparticle Films: Implications to Dye-Sensitized Solar Cells. *J. Phys. Chem. B* **2001**, *105*, 12433−12436.
(51) Kamat, P. V.; Christians, J. A.; Radich, J. G. Quantum Dot Solar Cells: Hole Transfer as a Limiting Factor in Boosting the Photoconversion Efficiency. *Langmuir* **2014**, *30*, 5716−5725.
(52) Katoh, R.; Furube, A. Electron Injection Efficiency in Dye-Sensitized Solar Cells. *J. Photochem. Photobiol., C* **2014**, *20*, 1−16.
(53) Bisquert, J.; Vikhrenko, V. S. Interpretation of the Time Constants Measured by Kinetic Techniques in Nanostructured Semiconductor Electrodes and Dye-Sensitized Solar Cells. *J. Phys. Chem. B* **2004**, *108*, 2313−2322.
(54) Abbas, M. A.; Basit, M. A.; Yoon, S. J.; Lee, G. J.; Lee, M. D.; Park, T. J.; Kamat, P. V.; Bang, J. H. Revival of Solar Paint Concept: Air-Processable Solar Paints for the Fabrication of Quantum Dot-Sensitized Solar Cells. *J. Phys. Chem. C* **2017**, *121*, 17658−17670.
(55) Bisquert, J.; Fabregat-Santiago, F.; Mora-Seró, I.; Garcia-Belmonte, G.; Barea, E. M.; Palomares, E. A Review of Recent Results on Electrochemical Determination of the Density of Electronic States of Nanostructured Metal-Oxide Semiconductors and Organic Hole Conductors. *Inorg. Chim. Acta* **2008**, *361*, 684−698.
(56) Bisquert, J. Chemical Diffusion Coefficient of Electrons in Nanostructured Semiconductor Electrodes and Dye-Sensitized Solar Cells. *J. Phys. Chem. B* **2004**, *108*, 2323−2332.
(57) Benkstein, K. D.; Kopidakis, N.; van de Lagemaat, J.; Frank, A. J. Influence of the Percolation Network Geometry on Electron Transport in Dye-Sensitized Titanium Dioxide Solar Cells. *J. Phys. Chem. B* **2003**, *107*, 7759−7767.
(58) Lin, H.; Huang, C. P.; Li, W.; Ni, C.; Shah, S. I.; Tseng, Y.-H. Size Dependency of Nanocrystalline TiO_2 on Its Optical Property and

https://dx.doi.org/10.1021/acsami.0c19352
ACS Appl. Mater. Interfaces 2021, 13, 6208−6218

Photocatalytic Reactivity Exemplified by 2-Chlorophenol. *Appl. Catal., B* **2006**, *68*, 1−11.
(59) Martinson, A. B. F.; Góes, M. S.; Fabregat-Santiago, F.; Bisquert, J.; Pellin, M. J.; Hupp, J. T. Electron Transport in Dye-Sensitized Solar Cells Based on ZnO Nanotubes: Evidence for Highly Efficient Charge Collection and Exceptionally Rapid Dynamics. *J. Phys. Chem. A* **2009**, *113*, 4015−4021.

https://dx.doi.org/10.1021/acsami.0c19352
ACS Appl. Mater. Interfaces 2021, 13, 6208−6218